# Multi-Octave Metamaterial Reflective Half-Wave Plate for Millimetre and Sub-Millimetre wave Applications

GIAMPAOLO PISANO,[1,*] BRUNO MAFFEI,[2] PETER A.R. ADE,[1] PAOLO DE BERNARDIS,[3] PETER DE MAAGT,[4] BRIAN ELLISON,[5] MANJU HENRY,[5] MING WAH NG,[1] BRIAN SCHORTT,[6] CAROLE TUCKER[1]

[1]*School of Physics and Astronomy, Cardiff University, CF24 3AA Cardiff, UK*
[2]*IAS, Université Paris-Sud, Orsay, 91405, France*
[3]*Dipartimento di Fisica, Universita' di Roma La Sapienza, 00185 Roma, Italy*
[4]*Electromagnetics & Space Environments Division, European Space Agency, NL 2200 AG Noordwijk, The Netherlands*
[5]*Rutherford Appleton Laboratory, Harwell Oxford, OX11 0QX Didcot, UK*
[6]*Future Missions Office, Science Directorate, European Space Agency, NL 2200 AG Noordwijk, The Netherlands*
**Corresponding author: giampaolo.pisano@astro.cf.ac.uk*

**The quasi-optical modulation of linear polarization at millimeter and sub-millimeter wavelengths can be achieved by using rotating half-wave plates (HWPs) in front of polarization sensitive detectors. Large operational bandwidths are required when the same device is meant to work simultaneously across different frequency bands. Previous realizations of half-wave plates, ranging from birefringent multi-plates to mesh-based devices, have achieved bandwidths of the order of 100%. Here we present the design and experimental characterization of a reflective HWP able to work across bandwidths of the order of 150%. The working principle of the novel device is completely different from any previous realization and it is based on the different phase-shift experienced by two orthogonal polarizations reflecting respectively off an electric conductor and an artificial magnetic conductor.**

**Journal reference**: "Multi-Octave Metamaterial Reflective Half-Wave Plate for Millimetre and Sub-Millimetre wave Applications," G. Pisano, B. Maffei, P.A.R. Ade, P. de Bernardis, P. de Maagt, B. Ellison, M. Henry, M.W. Ng, B. Schortt, C. Tucker, Applied Optics, 55, 10255-10262 (2016). DOI: 10.1364/AO.55.010255

## 1. Introduction

Millimetre and sub-millimetre wave polarimetric astronomical instruments have traditionally used rotating half-wave plates (HWPs) to identify linearly polarised components in an unpolarised scene [1, 2]. This methodology has multiple advantages: the modulation of the polarized signals can be moved to frequencies above any measurement 1/f noise; any polarimetric systematics of the optical components following the HWP can be removed [3, 4, 5, 6]; the source polarization angle can be determined independently from the sky scanning strategy. The work presented here is part of a Technology Research Programme (TRP) for the next generation of polarised Cosmic Microwave Background (CMB) radiation satellites, funded by the European Space Agency. The project aims to develop large diameter (1.2 metre) HWPs which meet with the requirements of the proposed Cosmic Origins Explorer (COrE) satellite instrument [7].

Historically, several different technologies have been employed to realise transmission HWPs, ranging from multi-plate birefringent designs [8, 9] to metamaterial based solutions [10, 11, 12, 13]. To minimise polarised systematics the COrE instrument design requires the first optical element to be the rotating HWP with a large (1.2 m) diameter. A practical reflective HWP solution was proposed based on rotating a free-standing wire-grid polariser in a plane parallel to that of the first mirror (Fig.1) [14, 15, 16]. This configuration satisfies the COrE instrument requirement to cover a large frequency range, from 60 to 600 GHz, but the fixed gap between the wire grid and mirror planes creates multiple narrow periodic bands which lowers the instantaneous sensitivity. Further, this also increases the complexity of the focal plane in accommodating these photometric bands. The challenges related to the development of such a large rotating device triggered the development of a completely different solution which is based on the mesh filters technology [17, 18].

We note that several types of reflective HWP modulators have been developed using a similar technology to that above: these are based on the translation of a wire-grid parallel to a mirror [19, 20, 21].

The novel design proposed here is based on a completely different working principle. The differential phase-shift between ordinary and extraordinary axes is neither achieved by mimicking a birefringent

material, nor by using Pancharatnam designs [8], nor capacitive or inductive grids and nor by a displacing wire-grid.
The new reflecting HWP is based on a simple observation; the phase change on reflection from a perfect electric conductor surface (PEC) is out of phase with that reflected from an artificial magnetic conductor (AMC) surface by π. Such AMC materials have been recently developed using the embedded mesh filter technology [22]. By combining the polarising grid with such an embedded AMC surface we can make an Embedded Reflective HWP (ER-HWP see Fig.2). Importantly, the usable bandwidth achieved by this new device is far superior to any other device realised in this field.

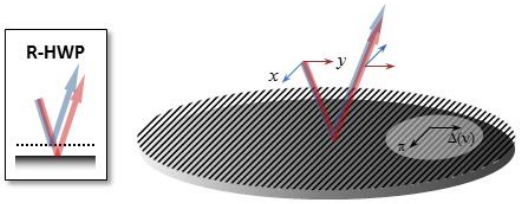


Fig. 1. Air-gap reflective HWP

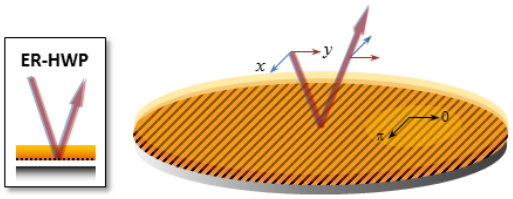


Fig. 2. Dielectrically embedded reflective HWP

## 2. Concept

In this section we compare and contrast different solutions by using one of the most important performance parameters for a HWP, the polarisation modulation efficiency. Assuming almost unitary reflection coefficient, we can define the modulation efficiency as $\varepsilon = sin^2(\Delta\phi/2)$, where $\Delta\phi$ is the differential phase-shift introduced by the HWP between the two orthogonal axes. Ideal modulation efficiencies are achieved when the HWP induces a differential phase-shift $\Delta\phi = \pi$.
Transmission line (TL) modelling [23] is used to investigate the normal incidence performance whereas more accurate finite element analysis [24] is necessary for modelling the off-axis cases and metamaterial structures. For a satellite CMB experiment such as COrE, the goal is to achieve high modulation efficiency (above 90%) across large bandwidths (of the order of 150% or more) whilst keeping the losses at low levels (<2%). In addition, the same performance has to be achievable for oblique incidence (angular stability up to 45° incidence angles).

### A. Traditional air-gap reflective HWP (R-HWP)

The traditional air-gap reflective HWP [14, 15, 16] consists of a free-standing wire-grid polariser parallel to a mirror with a specific air-gap, $d = \lambda_0/4$, where $\nu_0 = c/\lambda_0$ is the fundamental frequency [Fig. 3(a)]. The working principle is very simple. The polarisation component parallel to the grid is reflected whereas the orthogonal one goes through it, is reflected by the mirror and then recombines with the other polarisation. The extra path, equal to half a wavelength, adds a phase-shift equal to π at the frequency $\nu_0$. We have chosen $\nu_0 = 30$ GHz for our models.
The same phase-shift is also achieved at odd multiples of the fundamental frequency, $\nu_n = (2n+1)\nu_0$. However, at intermediate frequencies the phase-shift will deviate linearly from the ideal value and the modulation efficiency will vary sinusoidally, as shown in Fig. 4(a). This means that the plate is very efficient but only within narrow and periodic frequency bands. Due to this periodicity, the modulation efficiency can be calculated by averaging its value just across its first period, in this case in the range 0-60 GHz. This gives an $\varepsilon$ =0.5 which means that only 50% of the linearly polarised radiation will be modulated.
The manufacture of large diameter wire-grids is very challenging. The mechanical structures holding the wires have to be very strong and thus massive. This problem led us to investigate the following other options.

### B. Single-layer embedded R-HWP

It is possible to realise a simple embedded R-HWP based on the mesh-filters technology. The wire-grid can be replaced by a photolithographic version which is made by etching narrow copper strips on a polypropylene substrate. The substrate provides the required quarter-wavelength $\lambda_0/4n$ which is, in this case, within the dielectric medium of refractive index $n$ [Fig. 3(b)].
The presence of the dielectric substrate creates a mismatch for the radiation propagating in free-space. The overall effect is to decrease the modulation efficiency down to ~40% by narrowing down the periodic bands [Fig. 4(b)]. In addition, at non-normal incidence the modulation efficiencies for the *S*- and *P*- polarisations, respectively orthogonal and parallel to the plane of incidence, will not be equal, resulting in an unwanted inherent residual polarisation.

### C. Two-layer embedded R-HWPs

It is possible to reduce the mismatch introduced by the dielectric substrate discussed in part B by adding an anti-reflection coating layer [Fig. 3(c)]. This layer will have a lower refractive index equal to $n_{ARC} = \sqrt{n}$ and thickness equal to $\lambda_0/4n_{ARC}$. As shown in Fig. 4(c), in this case the overall efficiency goes back to almost ~50%.
We could add more coating layers in the attempt to improve the efficiency but, even in the perfectly matched case, the efficiency would not exceed 50% because it would be equivalent to completely embedding the free-standing R-HWP into a different medium.
It is clear from the above that none of the options discussed so far can achieve high efficiency or cover large bandwidths. In the following section we propose a completely different approach which can meet with our CMB experiment requirements.

### D. Multi-layer Embedded ER-HWP

What we are trying to achieve is an ideal surface, providing a differential phase-shift of π along two orthogonal directions. For the polarisation parallel to the wires, the wire-grid behaves almost like a perfect electric conductor (PEC) surface by providing an almost frequency-independent phase-shift of π. What is needed is something producing a null phase-shift in the direction orthogonal to the wires. In principle, this could be achieved if the device looked like an ideal perfect magnetic conductor (PMC) surface along that direction.
Even if PMC surfaces do not exist in nature, their behaviour is mimicked within certain bandwidths by the so called artificial magnetic conductor (AMC) surfaces [25]. Recently, a very large bandwidth AMC based on the mesh-filters technology has been developed at millimetre wavelengths [22]. In this device the null phase-shift is achieved by using internal reflection from a high-to-low refractive index interface. The radiation gets into the high index medium by means of a broadband antireflection coating. See reference [22] for a detailed analysis.
In the R-HWP design, a null phase-shift along the direction orthogonal to the wires can be then achieved if the radiation is gently brought into a high index medium and is then abruptly reflected off a high-to-low index interface. This can be achieved by a structure of the type sketched in Fig. 3(d). There are three layers with increasing refractive index, from

$n_1 \cong 1.25$ to $n_3 \cong 3$, followed by a lower index layer $n_4 \cong 1.5$ that could in principle be free-space.

Notice that the polarisation parallel to the wires will get into the high index medium and will be reflected by the wires as before [Fig 2], experiencing a $\pi$ phase-shift (PEC). The orthogonal polarisation will be almost completely reflected on the same plane by the high-to-low index interface which will provide a null phase-shift (AMC) over a large bandwidth. In contrast to the previous cases, both polarisation will now go through the same number of dielectric layers and will be reflected at the same plane [Fig. 2].

The polarisation modulation efficiency greatly increases up to an average of 80% between successive maxima. Within the regions around the peaks the efficiency is very high, around 99%, and very flat [Fig. 4(d)]. This is due to the flatness of the differential phase-shift achieved within the same bands.

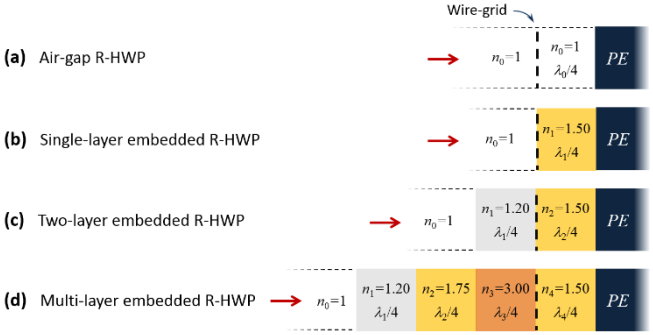


Fig. 3. Sketches of the different types of reflective HWPs.

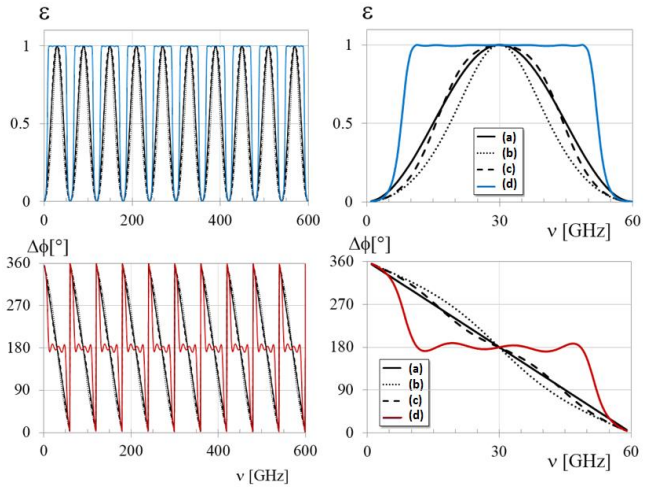


Fig. 4. Modulation efficiency and differential phase-shift for the different types of reflective HWPs (a), (b), (c) and (d) sketched in Fig. 3.

## 3. Modelling and Design

In this section we describe and model an Embedded Reflective ER-HWP based on a multi-layer AMC structure in more detail.

### A. Transmission line modelling

In the transition from the air-gap to the AMC-based R-HWP the periodic modulation efficiency changed from sinusoidal to a periodic top-hat shaped function (Fig. 4). This implies an increase of the relative bandwidth of the peaks. For example the fundamental peak has efficiency greater than 90% across a bandwidth of the order of 150%. This means that is possible to actually use just the first peak over a very large bandwidth simply by increasing the fundamental frequency $\nu_0$, i.e. by reducing the layer thicknesses.

The first layer has the lowest refractive index. This can be achieved with a material used for anti-reflection coatings, porous PTFE, which has a refractive index $n_1 \cong 1.25$ at millimetre wavelengths. The next layers are made by embedding meshes into polypropylene to create layers with refractive indexes of ~1.75 and ~3. The fourth layer could be an air-gap but we decided to use polypropylene, refractive index of $n_4 \cong 1.50$, which enables it to be mounted to a flat back plate for rigidity. This value is still much smaller than the last layer and is sufficient to guarantee the functioning of the AMC. Using a TL model the refractive indices for the other two quarter-wavelength layers were optimised to work about a frequency $\nu_0 = 240$ GHz. The required quarter wavelength layer refractive indices were determined to be $n_2 \cong 1.8$ and $n_3 \cong 3.0$.

### B. Artificial dielectric layers design

Two out of the four layers are made with low loss materials which are available at millimetre wavelengths. The second and the third layer require specific refractive indices which are not necessarily available. Using the mesh technology it is possible to engineer artificial dielectrics and a continuum of refractive indices can be achieved by embedding capacitive grids within polypropylene. The distance between the grids must be much smaller than the usual distances used in interference filters, meaning that they cannot be treated as individual lumped elements but rather as a whole structure which increases the refractive index of the supporting medium. This technique has been successfully used in the past to realise anti-reflection coatings [26].

The second and third layers have been designed individually using commercial Finite-Element Analysis (FEA) software [24]. The goal was to design two quarter-wavelength thick artificial slabs with refractive indices $n_2 \cong 1.8$ and $n_3 = 3.0$ starting from the lower index polypropylene substrate with $n_{PP} = 1.5$. The model consisted of a unit cell periodic structure with period $g$ much smaller than the minimum operational wavelength ($g$=100 μm). The mesh-loaded polypropylene slab was sandwiched between two semi-infinite slabs with the generic refractive index that we wanted to mimic (see inset Fig. 6). During the optimization procedure the number of grids, their geometry and their spacing were varied in order to minimize the reflection coefficient Γ, across the whole band. As shown in Fig. 5 the final reflection coefficients were both below -28 dB across the 10-490 GHz frequency range, meaning that the two artificial slabs were almost indistinguishable from homogeneous slabs with the targeted refractive indices. This result is expected in the limit where the meta-material pitch $g$ is small compared to the radiation wavelength.

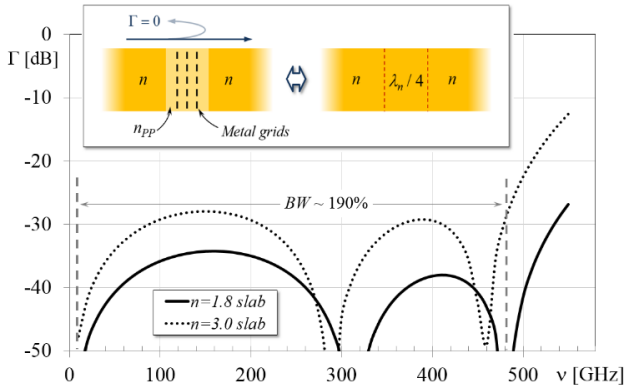


Fig. 5. Artificial dielectric layers model sketch and simulation results.

### C. Embedded R-HWP finite element design

Although the TL modelling provides a very good approximation of the optical performance of systems, a more detailed and accurate FEA model was required in order to include the details of the metamaterial structures. This FEA simulation only required a unit cell where homogeneous materials were used for the first and fourth layers, whilst the two optimized artificial dielectric layers had all their grid details inserted. The wire-grid was located within the high-to-low index interface. All the grids were modelled as copper with finite-conductivity. The frequency dependence of the polypropylene refractive index and loss tangent were taken into account using data from the in-house measurements [17, 27]. Master and slave periodic boundary conditions were used on the sides of the models to simulate infinitely extended slabs, thereby allowing off-axis incidence studies. The electromagnetic sources were plane-waves that could have arbitrary angles of incidence. We have defined the angle of incidence of the radiation $\vartheta$, the ER-HWP rotation angle $\alpha$ (null when the wire-grid is vertical) and the *S* and *P* polarizations (respectively perpendicular and parallel to the plane of incidence) as sketched in Fig. 6.

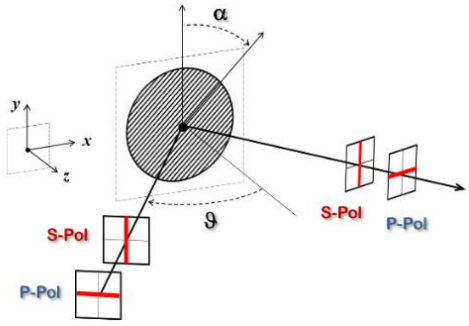


Fig. 6. Polarization and rotation angle definitions used in the ER-HWP models and tests.

The results of the finite-element on-axis simulations ($\vartheta$=0°) are reported in Fig. 7. Although the model now includes the metamaterial layers the expected performance is still close to ideal. Across the 76 - 383 GHz frequency range, corresponding to a fractional bandwidth of ~ 134%, the modulation efficiency is always above 90% and has an average value of 0.985. The efficiency calculation takes into account the losses and the phase error in the HWP. Within the same spectral region the differential phase-shift is kept within 176° ± 14° and along the two HWP axes ($\alpha$=0°, 90°) the averaged reflection and absorption coefficients are respectively of the order of 0.98 and 0.02

The finite-element model allowed the study of the reflective plate performance when the electromagnetic waves are incident at off-axis angles. In these cases it is necessary to distinguish between *S* and *P* polarizations and to account for the plate rotation angle $\alpha$. We have modelled incidence angles of $\vartheta$=22.5° and $\vartheta$=45°. The results will be discussed together with the associated measurements in Sec. 5.

We notice that the frequency range where the device operates (0 - 450 GHz) is well below its diffraction region for the grids used in the AMC structure. The diffraction limit is defined by the largest periodic structures of the device, in this case the grids constituting the artificial dielectric layers (100μm period). Taking into account the substrate refractive index and the incidence angles this limit is still well above 1 THz and so there is no diffraction or scattering due to the grid periodicities.

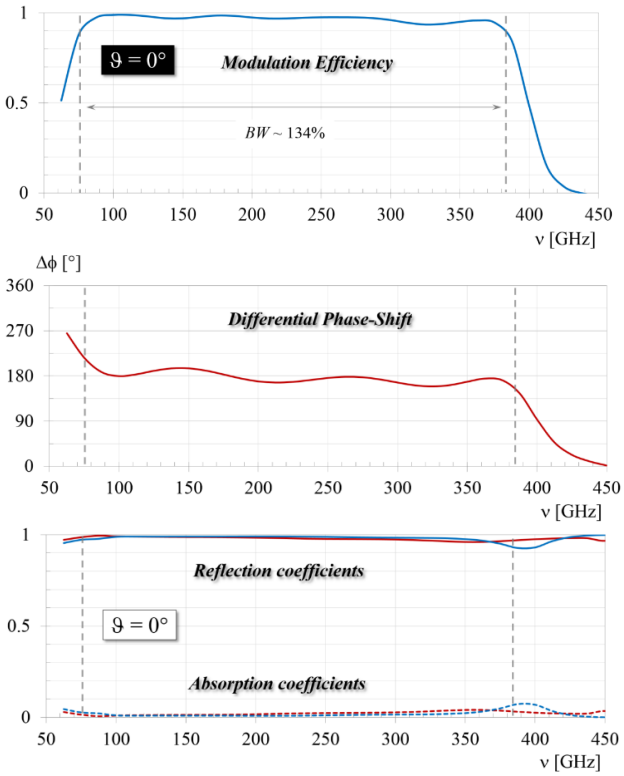


Fig. 7. On-axis ER-HWP finite element simulation results: (a) Reflection and absorption coefficients; (b) Differential phase-shift; (c) Modulation efficiency.

## 4. Manufacture

The device manufacture relies on the long-established metal-mesh production facilities at Cardiff University. Details of the hot-pressed metal-mesh technology have been reported in [17] and rely on lithographic and polymer-processing techniques to embed multiple mesh layers in precisely spaced dielectric substrates. The technology has been used for over 30 years for the production of quasi optical filters and polarizers for astronomical telescopes [28, 29].

The 200 mm diameter prototype device consisted of 4 patterned capacitive copper layers embedded in a 0.5 mm thick polypropylene support. The back surface was a 10 μm period polarizer separated from an inductive reflective layer. The device is shown in Fig. 8; it appears opaque due to the porous PTFE antireflection coating layer applied to the front surface as the final manufacture step.

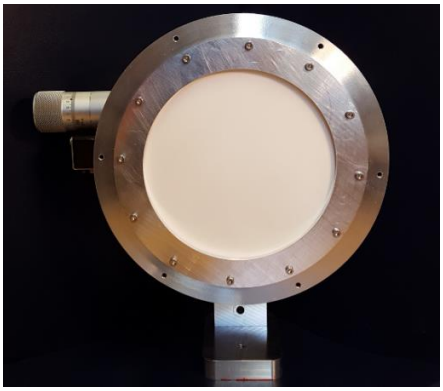

Fig. 8. Picture of the ER-HWP prototype, mounted in a rotary stage, tested in this work.

## 5. Experimental characterization

### A. Experimental configurations

To measure the spectral performance of the ER-HWP we used two Fourier Transform (FT) spectrometers: a Martin-Puplett polarising FTS [Fig. 9(a)] and a Mach-Zehnder FTS with the addition of two fixed polarisers [Fig. 9(b)].

The Martin-Puplett FTS uses a polarizing beam divider to achieve very large spectral coverage and contains fixed input and output polarisers so the beam incident at the ER-HWP has a fixed polarization state. However, rotation of the output polariser selects the orthogonal port of this spectrometer thus allowing both *S* and *P* measurements of the ER-HWP. Standard FT algorithms are used to get the reflection coefficients for each measurement. As a reference we replace the ER-HWP with a copper disc which allows determination of the spectral throughput of the FTS. A ratio of the device spectra against this background provides the inherent device reflectivity.

The Mach-Zehnder spectrometer uses an intensity metal mesh beam divider which covers about 4 octaves. For the instrument as configured here we optimised the response for the 120 – 480GHz region. To enable measurement of the ER-HWP we added two fixed polarisers as shown in Fig. 9(b) before and after the test plate. The simultaneous rotation of the two polarizers allowed tests with S and P polarizations.

In both cases a UV filtered mercury arc lamp thermal source was used in combination with a 1.5K Ge bolometric detector. The ER-HWP prototype was tested at room temperature.

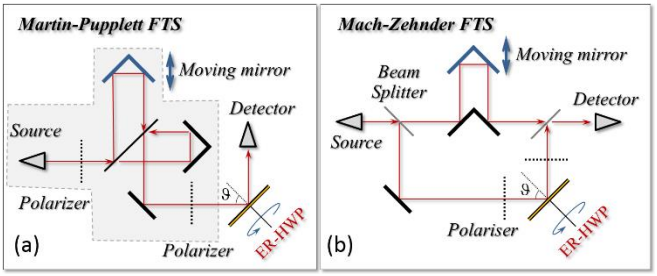


Fig. 9. a) Martin-Puplett polarising FTS, b) Mach-Zehnder FTS with two fixed polarisers. The placement of the ER-HWP is shown for both.

### B. Measurements and results

The ER-HWP was characterised at two incidence angles, $\vartheta$=22.5° and $\vartheta$=45°, using the Martin-Puplet setup shown in Fig. 9(a). In both cases two parallel wire-grid polarizers, located at the entrance and at the output of the interferometer, were able to define the polarization status of the incident radiation: *S* when the wires were horizontal; *P* when vertical. In each of the four previous configurations the waveplate reflection coefficients were acquired for three different rotation angles, $\alpha$=0°, 45°, 90°. These allowed characterization of the waveplate axes and its 45 degrees cross-polarization leakage.

The results of the $\vartheta$=22.5° and $\vartheta$=45° measurements are reported respectively in Fig. 10 and Fig. 11. In both cases, the reflection coefficients for the *S* and *P* polarization (a, b), the polarization modulation efficiency (c) and the differential phase-shift (d) as a function of frequency are superimposed to the finite element models expected performances. At the lowest frequencies the signal to noise ratio of the measurements is limited due to the rapidly decreasing source power (blackbody flux $\propto \nu^2$) and the sensitivity of the bolometric detector. The spectral structure near 100GHz shows this rapid increase in noise whereas at higher frequencies the spectral error ~1%. In addition, we note that these reflection measurements require normalization with a mirror replacing the ER-HWP which doubles the overall error.

The reflection measurements with the waveplate orientations $\alpha$=0, 90° give the reflection coefficients along its axes. These are interchanged between the *S* and *P* polarizations. The reflection coefficients are above 90% across about two octaves for both incidence angles and polarizations as expected by the relative model predictions.

In the $\alpha = 45°$ case the effect of the waveplate is to rotate the incoming linear polarization by 90° and, given the alignment of the two polarizers in the FTS, the signal is expected to be at its minimum. Using either the Jones or the Stokes formalism it is possible to show that the reflection coefficient is given by:

$$R_{45} = \frac{1}{4}(R_0 + R_{90} + 2\sqrt{R_0 \cdot R_{90}}\, cos\Delta\phi) \qquad (1)$$

In the case of identical reflection coefficients along the axes ($R_0 = R_{90}$) and ideal differential phase-shift ($\Delta\phi = \pi$) we would not expect to detect any signal in the original direction. However, the observed cross-polarization leakage provides information about the polarization modulation efficiency. We can define this as follows:

$$\varepsilon = R_0 - R_{45} \qquad (2)$$

This equation, valid for any $\vartheta$, *S* and *P*, informs on that fraction of the signal, which was initially aligned and reflected along one axis, which has been rotated by 90° when the plate axes are positioned at 45° to the incoming polarization. The modulation efficiencies for the *S* and *P* polarizations are different but still very similar. We report the average of them in Fig. 10(c) and Fig.11(c). We see that the modulation efficiencies are above 90% across roughly two octaves and that the bandwidth gets larger by increasing the angle of incidence $\vartheta$.

FTS measurements carried out with a standard instrument configuration, as sketched Fig. 9(a), do not provide phase information directly. In order to extract the differential phase-shift between the waveplate axes we need to combine the previous three measurements. This can be done by rearranging equation (2) and obtaining:

$$\Delta\phi = \pm arccos\left[\frac{2R_{45} - 0.5(R_0 + R_{90})}{\sqrt{R_0 R_{90}}}\right] \qquad (3)$$

The differential phase-shift for the $\vartheta$=22.5° measurements extracted using equation (3) are reported in Fig. 10(d). Given the *arccos* function sign indeterminacy the phase can appear either all above or all below 180°. Knowing the model predictions we have manually attributed the negative sign to the data below 175 GHz (see dotted line in Fig. 10(d)). We notice that in this method any random noise detected by the FTS at $\alpha = 45°$ results in a systematic error which forces the phase to depart from 180°.

For the above reasons in the $\vartheta$=45° case we have used a completely different experimental configuration to measure the differential phase-shift. The modified Mach-Zehnder FTS described earlier and sketched in Fig. 9(b) allows direct measurements of the phase without any sign indeterminacy. In addition, it does not rely on the $\alpha = 45°$ cross-polarization measurements with the associated noise problems discussed above. The phase-shift is obtained directly by computing the complex Fourier Transforms of the inteferograms at $\alpha = 0°$ and $\alpha = 90°$, by taking their frequency dependent arguments and subtracting them, as described in more detail in [22]. The differential phase-shifts computed for both the *S* and *P* polarisations are seen to be very close to the model predictions across two octaves (Fig. 11(d)). As with the standard FTS configuration, these data are limited by source flux which is a factor of 2 smaller for our M-Z system. However, since we do not replace the test device with a mirror the systematic error for the phase measurement is reduced compared to the M-P system. The overall errors of the two techniques are thus comparable.

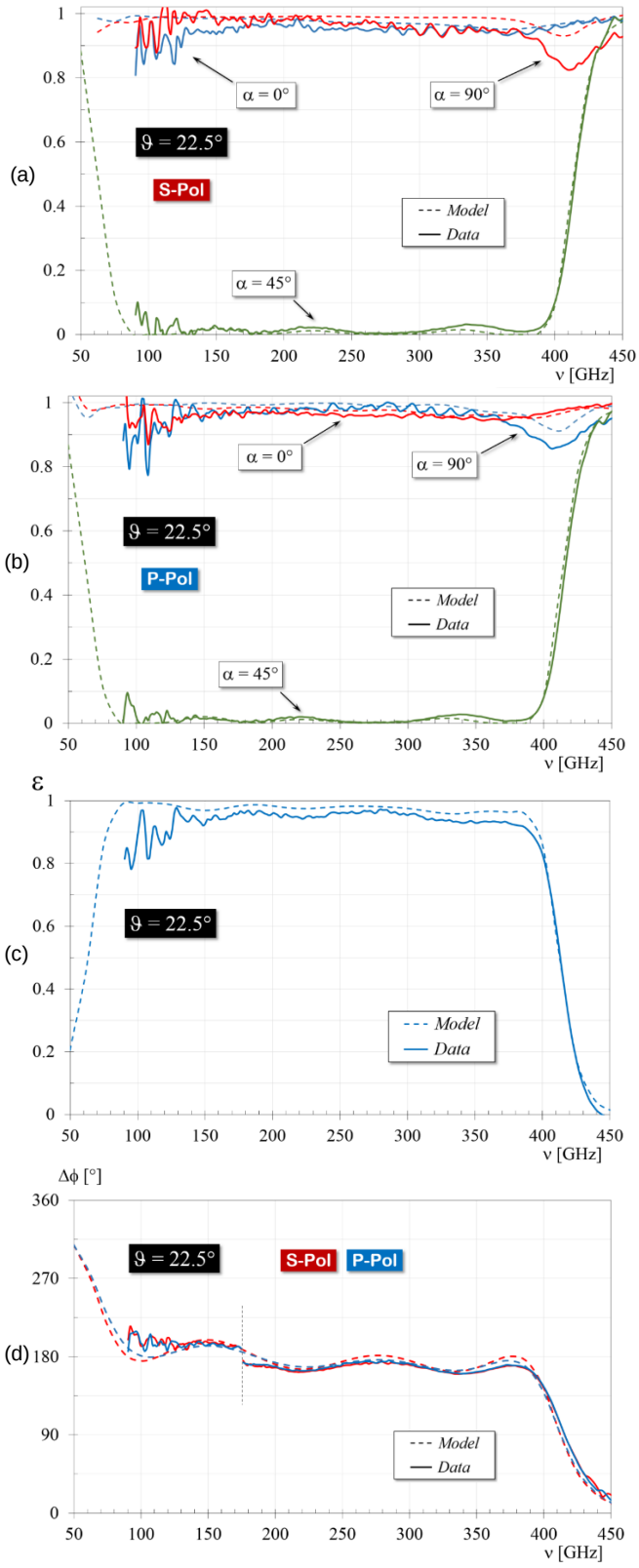


Fig. 10. Off-axis measurements vs model predictions at ϑ=22.5° incidence angle. (a, b) S- and P-polarization reflection coefficients at α=0°, 45°, 90° rotation angles; (c) Averaged S- and P-polarization modulation efficiency. (d): Martin-Puppletl FTS differential phase-shifts. The dashed line defines the frequency below which we have manually attributed the negative sign to the data.

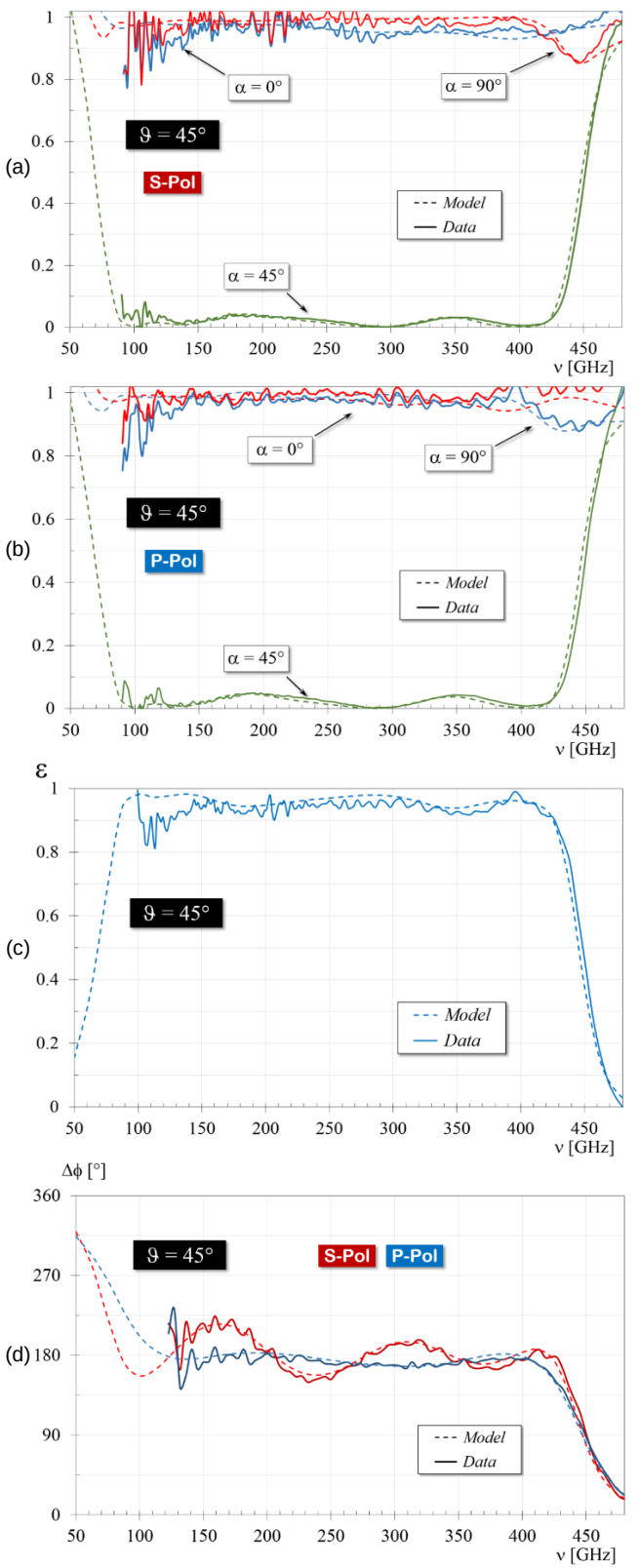


Fig. 11. Off-axis measurements vs model predictions at ϑ=45° incidence angle. (a, b) S- and P-polarization reflection coefficients at α=0°, 45°, 90° rotation angles; (c) Averaged S- and P-polarization modulation efficiency. (d): Mach-Zehnder FTS differential phase-shifts.

## 5. Conclusions

We have developed a new type of reflective HWP based on metamaterials. The working principle is completely different from any previous designs and is based on the different phase-shifts experienced by the orthogonal polarizations reflecting off either an electric conductor or an artificial magnetic conductor.

A prototype working across the frequency range ~100-400 GHz has been manufactured using the mesh-filter technology and tested with two Fourier Transform Spectrometers. The polarisation modulation efficiency is observed to be greater than 90% over a bandwidth of two octaves. The ER-HWP shows good angular stability by maintaining similar performances across the same operational bandwidth for incidence angles up to 45°. The differential phase-shift oscillates around 180°, within ±20° and ±30° respectively for the $\vartheta$=22.5° and $\vartheta$=45° incidence angles.

The above performance has never been achieved before and exceeds the limits of both birefringent multi-plate Pancharatnam designs and the transmission mesh HWPs. Larger bandwidths can be achieved by increasing the number of layers in the gradient index section and also by increasing the value of the refractive index of the last layer.

Whilst this development was driven by the requirements of the COrE CMB satellite we note that it also offers significant advantages for other polarimetric instruments.

**Funding Information.** European Space Agency (ESA) contract number 4000107865/13/ML/MH.

**Acknowledgment**.

The Authors acknowledge support from the European Space Agency through a Technology Research Program.

## References

1. J. Tinbergen, Astronomical Polarimetry, Cambridge University, 1996
2. R. H. Hildebrand, J. A. Hildebrand, J. L. Dotson, C. D. Dowell, G. Novak, and J. E. Vaillancourt, "A primer on far-infrared polarimetry," Publ. Astron. Soc. Pac. 112, 1215–1235 (2000).
3. S. A. Bryan, T. E. Montroy, and J. E. Ruhl, "Modeling dielectric half-wave plates for cosmic microwave background polarimetry using a Mueller matrix formalism," Appl. Opt. 49, 6313–6323 (2010).
4. Essinger-Hileman, T., Kusaka, A., Appel, J.W., Choi, S.K., Crowley, K., Ho, S.P., Jarosik, N., Page, L.A., Parker, L.P., Raghunathan, S., Simon, S.M., Staggs, S.T., Visnjic, K., "Systematic effects from an ambient-temperature, continuously rotating half-wave plate", Review of Scientific Instruments, 87, 094503 (2016).
5. Kusaka, A., Essinger-Hileman, T., Appel, J. W., Gallardo, P., Irwin, K. D., Jarosik, N., Nolta, M. R., Page, L. A., Parker, L. P., Raghunathan, S., Sievers, J. L., Simon, S. M., Staggs, S. T., Visnjic, K., "Modulation of cosmic microwave background polarization with a warm rapidly rotating half-wave plate on the Atacama B-Mode Search instrument", Review of Scientific Instruments, 85, 024501 (2014).
6. B. R. Johnson, J. Collins, M. E. Abroe, P. A. R. Ade, J. Bock, J. Borrill, A. Boscaleri, P. de Bernardis, S. Hanany, A. H. Jaffe, T. Jones, A. T. Lee, L. Levinson, T. Matsumura, B. Rabii, T. Renbarger, P. L. Richards, G. F. Smoot, R. Stompor, H. T. Tran, C. D. Winant, J. H. P. Wu. J. Zuntz, "MAXIPOL: Cosmic Microwave Background Polarimetry Using a Rotating Half-Wave Plate", 2007, The Astrophysical Journal, 665:1 42
7. The COrE Collaboration, "COrE (Cosmic Origins Explorer) A White Paper", arXiv:1102.2181 (2011)
8. S. Pancharatnam, "Achromatic combinations of birefringent plates—Part II. An achromatic quarter wave plate," Proc. Indian Acad. Sci. A 42, 24–31 (1955).
9. G. Pisano, G.Savini, P.A.R.Ade, V.Haynes and W.K. Gear, "Achromatic Half-Wave Plate for Submillimetre Instruments in CMB Astronomy: Experimental Characterisation," Appl. Opt. **45**, 6982-6989 (2006).
10. P. A. R. Ade, D. T. Chuss, S. Hanany, V. Haynes, B. G. Keating, A. Kogut, J. E. Ruhl, G. Pisano, G. Savini, and E. J. Wollack, "Polarization modulators for CMBPol," J. Phys. Conf. Ser. 155, 012006 (2009).
11. G. Pisano, G. Savini, P.A.R. Ade, V. Haynes, "A Metal-mesh Achromatic Half-Wave Plate for use at Submillimetre Wavelengths," Appl. Opt. **47**, 6251-6256 (2008).
12. G.Pisano, M. W. Ng, V. Haynes and B. Maffei, "A Broadband Metal-Mesh Half-Wave Plate for Millimetre Wave Linear Polarisation Rotation," Progress In Electromagnetics Research M, **25**, pp.101-114 (2012)
13. G. Pisano, B. Maffei, M.W. Ng, V.Haynes, M. Brown, F. Noviello, P. de Bernardis, S. Masi, F. Piacentini, L. Pagano, M. Salatino, B. Ellison, M. Henry, P. de Maagt, B. Shortt, "Development of Large Radii Half-Wave Plates for CMB satellite missions," Proceedings of the SPIE, **9153**, id. 915317 (2014).
14. H. Shinnaga, M. Tsuboi and T. Kasuga, "A Millimeter Polarimeter for the 45-m Telescope at Nobeyama," Publ. Astron. Soc. Japan 51, 175-184 (1999).
15. G. Siringo, E. Kreysa, L. A. Reichertz and K. M. Menten, "A new polarimeter for (sub)millimeter bolometer arrays," Astronomy & Astrophysics 422, 751–760 (2004).
16. P. F. Goldsmith, Quasioptical Systems, pp. 198-199, IEEE, (1998).
17. P. A. R. Ade, G. Pisano, C. E. Tucker, S. O. Weaver, "A Review of Metal Mesh Filters," Proceedings of the SPIE, **6275**, pp.U2750 (2006).
18. G. Pisano, P. Ade, C. Tucker, P. Moseley and M.W. Ng, "Metal mesh based metamaterials for millimetre wave and THz astronomy applications", Proceedings 8th UCMMT-2015 Workshop Cardiff, pp.1-4 (2016).
19. D. T. Chuss, et al., "Interferometric polarization control," Appl. Opt. 45, 5107–5117 (2006).
20. D. T. Chuss, et al., "Properties of a variable- delay polarization modulator," Appl. Opt. 51, 197–208 (2012).
21. D. T. Chuss, E. J. Wollack, G. Pisano, S. Ackiss, K. U-Yen, and M.W. Ng, "A translational polarization rotator," Appl. Opt. 51, 6824-6830 (2012).
22. G. Pisano, P. A. R. Ade, C, Tucker, "Experimental realization of an achromatic magnetic mirror based on metamaterials," Appl. Opt. **55**, 4814-4819 (2016).
23. P. Yeh, Optical Waves in Layered Media, Chap. 5, Wiley (1988).
24. High Frequency Structure simulator (HFSS): www.ansys.com
25. C.R. Brewitt-Taylor, "Limitation on the bandwidth of artificial perfect magnetic conductor surfaces," IET Micr. Ant. Prop. **1**, 255–260 (2007).
26. Zhang, J., Ade, P.A.R, Mauskopf, P., Moncelsi, L., Savini, G. and Whitehouse, N., "New Artificial Dielectric Metamaterial and its Application as a THz Anti-Reflection Coating," Appl. Opt. **48**, 6635-6642 (2009).
27. Tucker, C. E.; Ade, P. A. R."Thermal filtering for large aperture cryogenic detector arrays", Proceedings of the SPIE, **6275**, pp. 62750T, (2006).
28. P. A. R. Ade, G. Savini,, R. Sudiwala, C. Tucker, A. Catalano, S. Church, R. Colgan, F. X. Desert, E. Gleeson, W.C. Jones, J.-M. Lamarre, A. Lange, Y. Longval, B. Maffei, J. A. Murphy, F. Noviello, F. Pajot, J.-L. Puget, I. Ristorcelli, A. Woodcraft, and V. Yurchenko, "Planck pre-launch status: The optical architecture of the HFI", Astronomy & Astrophysics v.520, A11 (2010).
29. M.J. Griffin et al., "The Herschel-SPIRE instrument and its in-flight performance", Astronomy & Astrophysics, v. 518(4), id.L3 (2010).